Bio-Design and Manufacturing (2025) 8:800–818
https://doi.org/10.1631/bdm.2400495

RESEARCH ARTICLE

Silk fibroin bandage for preventing tendon adhesions

Pengcheng Xia[2] · Guofeng Liu[1,3,4] · Tianhong Qiao[1,3,4] · Ke Yao[1,3,4] · Chaofan He[1,3,4] · Yong He[1,3,4,5] · Jianchao Gui[2] · Yuan Sun[1,3,4,5]

Received: 9 December 2024 / Accepted: 23 March 2025

Abstract

Tendon adhesion, a prevalent complication affecting over 30% of patients after a tendon injury or surgery, results in joint stiffness and impaired mobility. Although current treatments facilitate tendon repair, they are often insufficient in preventing adhesions and promoting optimal healing outcomes. To address these challenges, we developed an oriented cryostructured silk fibroin bandage (OCSFB) using the directional freeze-casting methodology. In vitro studies demonstrated that OCSFB provided a favorable microenvironment for cell viability, proliferation, and alignment, concurrently upregulating the expression of tendon-specific genes. In a rat Achilles tendon model, OCSFB significantly reduced adhesion formation and improved tendon healing. RNA-seq analysis further revealed modulation of cell adhesion molecules, substantiating its role in tissue regeneration. The integration of silk fibroin biocompatibility with a unique microstructure that facilitates cellular adhesion and proliferation renders OCSFB a promising approach for mitigating tendon adhesions and improving repair outcomes, establishing it as a robust candidate for clinical application.

Pengcheng Xia, Guofeng Liu, and Tianhong Qiao have contributed equally to this work.

✉ Jianchao Gui
gui1997@126.com

✉ Yuan Sun
yuansun@zju.edu.cn

[1] State Key Laboratory of Fluid Power and Mechatronic Systems & Liangzhu Laboratory, School of Mechanical Engineering, Zhejiang University, Hangzhou 310027, China

[2] Department of Orthopaedics, Nanjing First Hospital, Nanjing Medical University, Nanjing 210006, China

[3] The Second Affiliated Hospital, Zhejiang University School of Medicine, Hangzhou 310027, China

[4] Key Laboratory of 3D Printing Process and Equipment of Zhejiang Province, School of Mechanical Engineering, Zhejiang University, Hangzhou 310027, China

[5] Dr. Li Dak Sum & Yip Yio Chin Center for Stem Cells and Regenerative Medicine, Zhejiang University, Hangzhou 310027, China

Graphical abstract

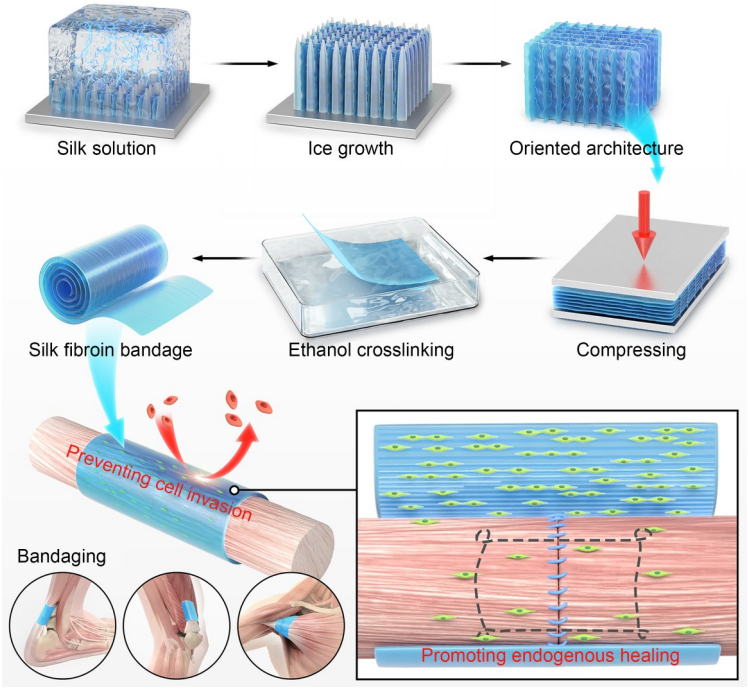

Keywords Silk fibroin · Directional freeze-casting · Biomaterials · Tendon adhesion · Tendon healing

1 Introduction

Tendon adhesion, which affects over 30% of patients after tendon injuries or surgical interventions, is a prevalent and challenging complication that poses significant clinical and economic burdens [1]. This condition is characterized by the development of aberrant fibrous linkages between the tendon and surrounding tissues, severely impairing the natural gliding motion vital for optimal joint function [2–4]. These restrictions cause joint rigidity, discomfort, and significant functional limitations, adversely affecting the quality of life of the patient and imposing a substantial economic strain on individuals and society [5–7].

An effective strategy for mitigating tendon adhesion must address several essential prerequisites [5, 8, 9]. Primarily, it is crucial to establish a physical barrier that prevents the entry of external inflammatory cells and fibroblasts from nearby tissues into the injury area [10, 11]. This barrier should exhibit sufficient mechanical integrity to withstand physiological movements without incurring damage or deformation throughout the healing process. Moreover, facilitating the functional healing of the tendon is of paramount importance. The therapeutic intervention should promote intrinsic tendon repair by guiding cellular alignment and tissue organization, ensuring that the regenerated tendon exhibits appropriate biomechanical properties. Finally, it is imperative to regulate the degradation rate of the barrier material in synchronization with the timeline of tendon healing [12–14]. The material should provide mechanical support during critical stages of recovery and subsequently degrade in a controlled manner to prevent long-term foreign body reactions and eliminate the need for surgical removal [15].

The achievement of these standards is dependent on the crucial roles of material choice and structural design. The biopolymer silk fibroin (SF), extracted from silkworm cocoons, has emerged as a promising material due to its excellent biocompatibility, favorable mechanical properties, controllable degradation rates, and ease of processing [16–20]. Compared with synthetic polymers such as polylactic acid and polycaprolactone (PCL), SF exhibits superior cellular affinity and induces minimal inflammatory responses, making it an ideal candidate for tendon repair applications [11, 21–23]. The mechanical properties of SF closely resemble those of the native tendon tissue, thereby providing essential structural support. Furthermore, SF can be processed into diverse forms with tailored microarchitectures, rendering it particularly suitable for applications in tissue engineering [19, 20, 24]. Regarding the structural design, the incorporation of aligned microscale or nanoscale features into the barrier material provides physical cues that guide tendon cell growth and

alignment. Advanced techniques such as directional freeze-casting enable the fabrication of scaffolds with oriented porous structures that replicate the highly organized collagen fiber architecture of native tendons. By emulating the native tendon microenvironment, these oriented structures promote the ordered regeneration of the tendon tissue and facilitate intrinsic healing. This approach has the potential to accelerate healing, reduce complications, and improve functional outcomes [19, 25–27].

This study describes the development of a novel oriented cryostructured silk fibroin bandage (OCSFB) fabricated by directional freeze-casting (Fig. 1). The engineered bandage exhibits a unique aligned microstructure without the need for exogenous chemical crosslinkers or bioactive compounds. The OCSFB effectively prevents external cellular infiltration through physical isolation and promotes tendon healing by guiding cell alignment and tissue organization via its oriented structure. In addition to serving as a physical barrier, OCSFB improves tendon healing by guiding cell alignment and tissue organization. This is further supported by comprehensive material characterization, which demonstrated its superior microstructural organization and mechanical properties compared to those of an unoriented cryostructured silk fibroin bandage (UCSFB). In vitro analyses revealed that OCSFB exhibited excellent cell viability, proliferation, and hemocompatibility; improved the cellular alignment; significantly upregulated the expression of collagen (types I and III, i.e., *COL1* and *COL3*) and tendon-related genes (*COL1A1*, *COL3A1*, tenascin-C (*TNC*), and tenomodulin (*TNMD*)). The efficacy of OCSFB was validated using a rat Achilles tendon injury model, where comprehensive evaluations, including histological, gait, and mechanical analyses, collectively demonstrated superior anti-adhesion effects and tendon-healing capabilities to those in the UCSFB and control groups. Moreover, RNA-seq analysis identified significant differences in gene expression profiles, specifically in the regulation of cell adhesion molecules (CAMs), further supporting the potential of OCSFB to promote tissue regeneration and prevent adhesion formation.

The innovative aspect of this study lies in the strategic integration of material selection and structural design, addressing the critical limitations of existing anti-adhesion strategies. Through a systematic multifaceted evaluation, this study demonstrated that the oriented microstructure achieved by directional freeze-casting conferred OCSFB with superior structural organization and biological performance. The aligned architecture of the scaffold facilitates tenocyte alignment and extracellular matrix (ECM) deposition, thereby

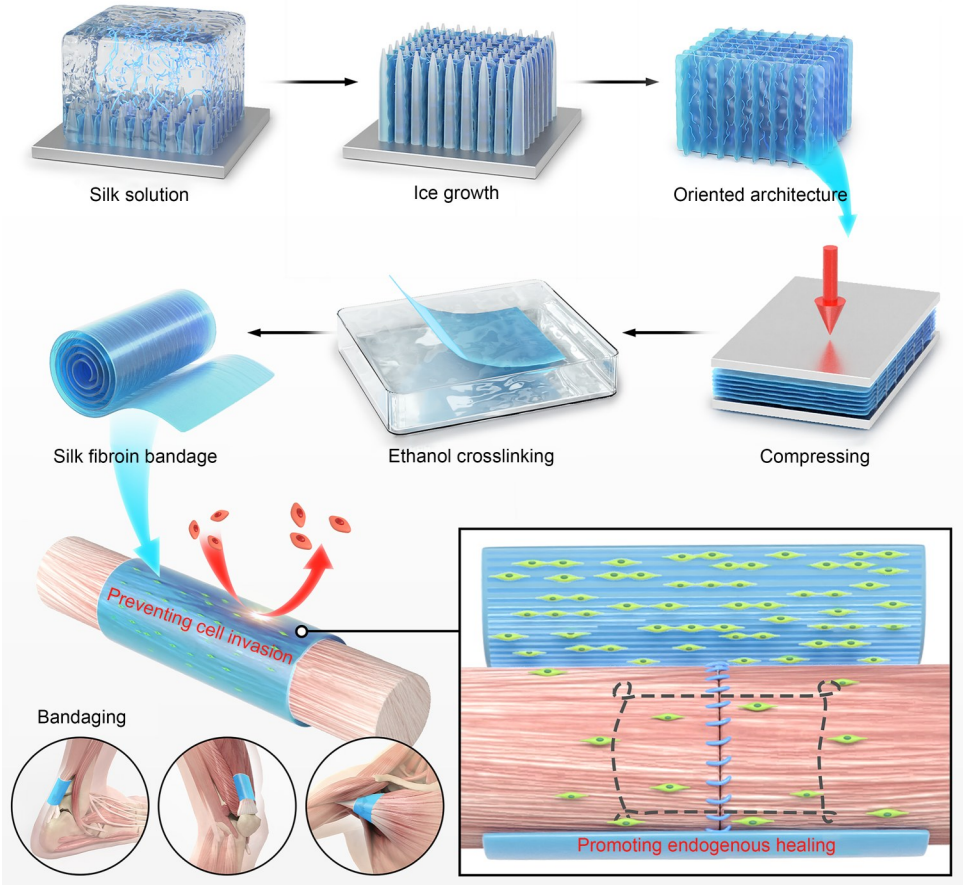

Fig. 1 Preparation and application of the oriented cryostructured silk fibroin bandage

increasing the expression of tendon-specific markers. In vivo experiments using a rat Achilles tendon injury model validated the therapeutic efficacy of OCSFB, demonstrating superior anti-adhesion performance and improved tendon healing through comprehensive histological, biomechanical, and functional analyses. RNA-seq analysis clarified the molecular mechanisms by which OCSFB modulates cell adhesion-related pathways, thereby providing mechanistic insights into its therapeutic effects. These comprehensive evaluations demonstrate the potential of OCSFB as an innovative approach for preventing postoperative tendon adhesion and promoting functional tissue regeneration, suggesting promising prospects for clinical translation.

2 Results

2.1 Fabrication and structural characterization of OCSFB versus unoriented silk fibroin bandages

We fabricated two types of SF bandages using distinct freezing methodologies, viz., OCSFB by directional freeze-casting at − 90 °C and UCSFB by conventional isotropic freezing. For OCSFB, we investigated SF concentrations of 2%, 4%, 6%, and 10% (mass fraction); for UCSFB, SF was prepared at a mass fraction of 2%. Both bandage types underwent sequential post-processing, including freeze-drying, mechanical compression, and ethanol treatment for structural stabilization.

At a mass fraction of 2%, OCSFB exhibited microfibers with diameters of (1.72±0.11) μm and interfiber spacings of (10.83±0.35) μm, which were unidirectionally aligned (Table S1 in the supplementary information). Energy-dispersive X-ray spectroscopy (EDS) analysis confirmed the presence of carbon, oxygen, nitrogen, and sulfur (Table S2 in the supplementary information), and the EDS images showed that the compressed OCSFB exhibited a more compact structure (Fig. 2b). With an increase in the concentration of SF, OCSFB transitioned from fibrous to sheet-like structures, whereas UCSFB, resulting from isotropic freezing, exhibited random morphologies. Macroscopically, OCSFB demonstrated increased stiffness and compactness with increasing concentrations, as depicted in Fig. 2a. UCSFB demonstrated irregular morphologies, whereas OCSFB exhibited consistent alignment. The dimensions and thickness of the bandages increased proportionally with concentration, as confirmed by scanning electron microscopy (SEM) images. Mechanical characterization demonstrated that directional freezing significantly improved the scaffold strength, with 2% OCSFB showing a tensile modulus of (3.22±0.08) MPa, approximately 5-fold higher than that shown by 2% UCSFB ((0.62±0.15) MPa) (Table S3 in the supplementary information). The tensile modulus of OCSFB further increased with concentration, reaching (18.31±1.20) MPa at 10%. Nevertheless, considering the balance between sufficient mechanical integrity and appropriate flexibility for tendon wrapping applications, we selected 2% OCSFB as the optimal formulation for subsequent experiments, with 2% UCSFB serving as the control. Figure 2c illustrates the macroscopic photographs of UCSFB and OCSFB at various concentrations. Higher SF concentrations in OCSFB resulted in increased stiffness and compactness, supporting its use as a tendon repair material. Figure 2d depicts the simulated application scenario for both 2% UCSFB and 2% OCSFB, emphasizing their potential use in preventing tendon adhesions and promoting healing.

Small-angle X-ray scattering (SAXS) analysis revealed random orientation in UCSFB but strong unidirectional alignment in OCSFB (Fig. 2e). The azimuthal intensity distribution for OCSFB displayed sharp peaks at 90° and 270°, confirming the alignment along the freezing direction (Fig. 2f). Wide-angle X-ray scattering (WAXS) analysis indicated low crystallinity in both UCSFB and OCSFB before crosslinking (Fig. 2g). After ethanol treatment, both samples exhibited increased β-sheet formation, as evidenced by the clearer scattering rings and higher scattering intensity (Fig. 2h).

Multiple complementary analyses confirmed that ethanol crosslinking improved the scaffold stability through β-sheet formation. Thermogravimetric analysis (TGA) and differential scanning calorimetry (DSC) revealed reduced moisture content and improved thermal stability in crosslinked samples (Figs. 2i and 2j), and X-ray diffraction (XRD) showed intensified β-sheet peaks at 20.2° and 24.2° (Fig. 2k). Fourier transform infrared (FTIR) spectroscopy further validated this structural transition through characteristic shifts in amide I and II peaks (Fig. 2l). These molecular changes occurred without disrupting the distinct microstructural alignment patterns established during the freezing process.

2.2 Scaffold preparation, cell viability, hemocompatibility, and cellular alignment on UCSFB and OCSFB

UCSFB and OCSFB were cut into shapes and sizes appropriate for various assays (Fig. 3a), which ensured compatibility with cell culture, mechanical testing, and biocompatibility evaluations. Live/Dead staining (Fig. 3b) revealed that UCSFB and OCSFB supported cell attachment and survival. There were no significant differences in cell density between the two bandages at any time point. Although there was a slightly higher density of live cells on OCSFB scaffolds by Day 7, this difference was not statistically significant. Quantitative analysis by live/dead staining (Fig. 3d) also showed no statistically significant differences in cell viability, indicating biocompatibility and lack of cytotoxicity for both bandages. The cell counting kit-8 (CCK-8) assay

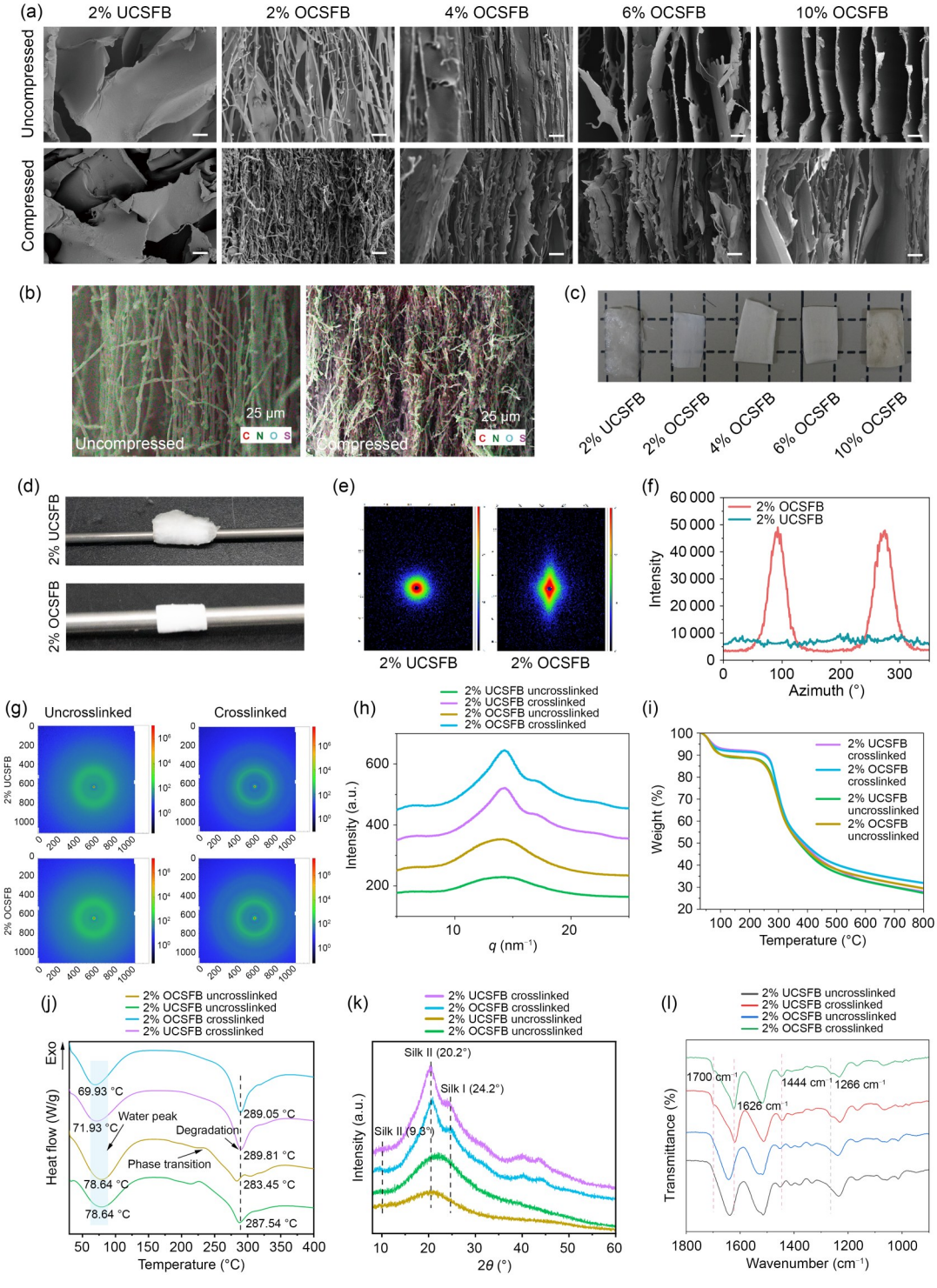

Fig. 2 Fabrication and structural characterization of oriented versus unoriented silk fibroin bandages. (a) SEM images of 2% UCSFB and 2%, 4%, 6%, and 10% OCSFB before and after mechanical compression (scale bars: 10 μm). (b) EDS mapping of 2% OCSFB before and after compression. (c) Macroscopic photographs of 2% UCSFB and 2%, 4%, 6%, and 10% OCSFB. (d) Schematic illustration demonstrating the simulated application scenario for 2% UCSFB and 2% OCSFB. (e) SAXS patterns of 2% UCSFB and 2% OCSFB. (f) Azimuthal intensity plots from SAXS data for 2% UCSFB and 2% OCSFB. (g) WAXS patterns of 2% UCSFB and 2% OCSFB before and after ethanol crosslinking (the horizontal and vertical axes correspond to the pixel coordinates of the two-dimensional detector, while the scale bar indicates the scattering intensity). (h) WAXS intensity profiles as a function of the scattering vector $\boldsymbol{q}$ for 2% UCSFB and 2% OCSFB before and after ethanol crosslinking ($q=4\pi\cdot\sin\theta/\lambda$). (i) Thermogravimetric (TG) curves of 2% UCSFB and 2% OCSFB before and after ethanol crosslinking. (j) DSC curves of 2% UCSFB and 2% OCSFB before and after ethanol crosslinking. (k) XRD patterns of 2% UCSFB and 2% OCSFB before and after ethanol crosslinking. (l) FTIR spectroscopy spectra of 2% UCSFB and 2% OCSFB before and after ethanol crosslinking

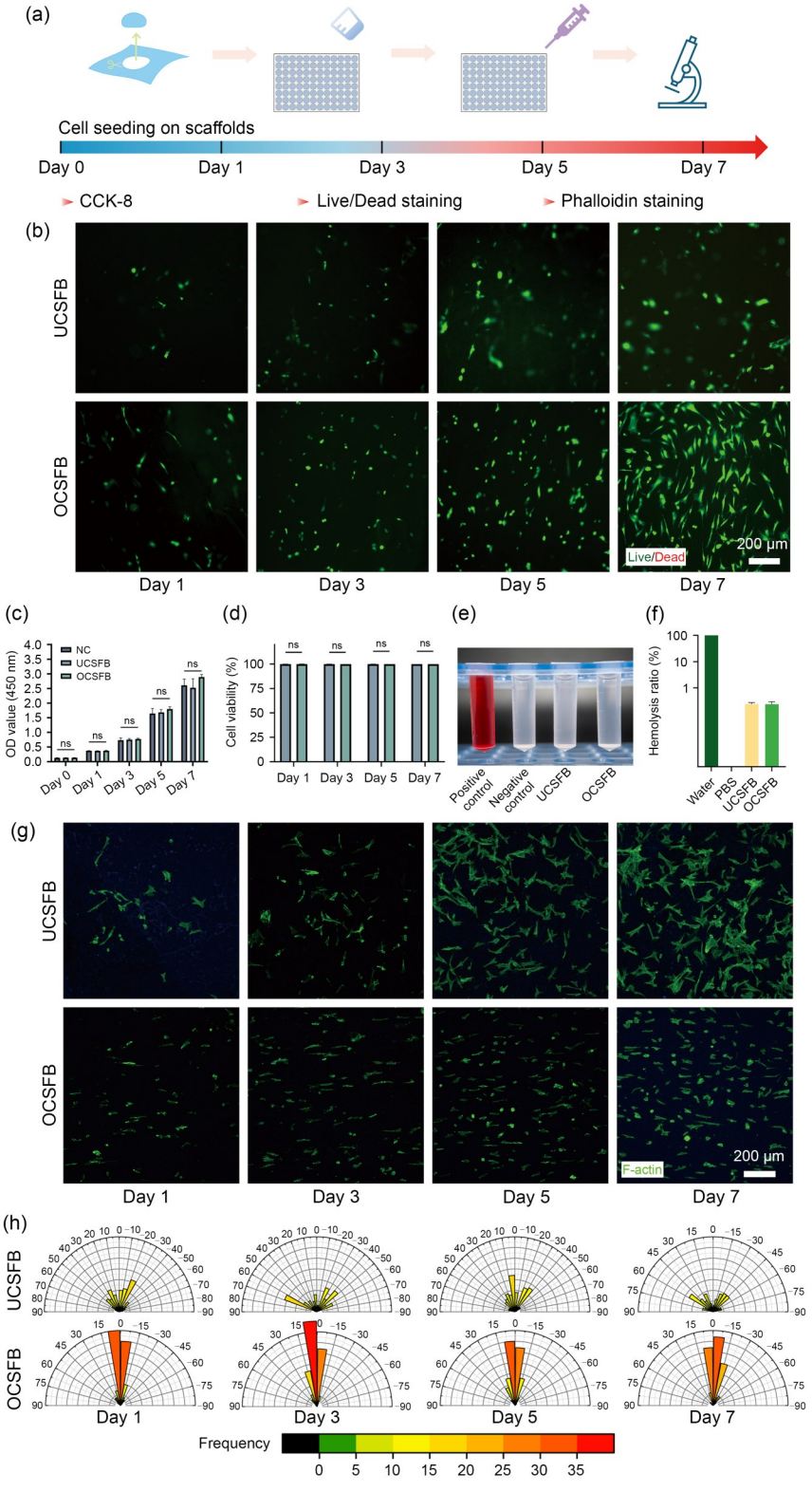

Fig. 3 Scaffold preparation, cell viability, hemocompatibility, and cellular alignment on UCSFB and OCSFB. (a) Schematic of the preparation process of UCSFB and OCSFB scaffolds, with both types being cut into appropriate sizes for various assays. (b) Live/Dead staining of cells cultured on UCSFB and OCSFB scaffolds at Days 1, 3, 5, and 7 (scale bar: 200 μm). (c) CCK-8 assay results demonstrating cell proliferation on UCSFB and OCSFB over 7 d (NC: negative control). (d) Quantitative analysis of cell viability based on live/dead staining. (e) Hemolysis test comparing hemocompatibility between UCSFB and OCSFB. (f) Quantification of hemolysis rates. (g) Phalloidin staining of the cytoskeleton on UCSFB and OCSFB after 7 d of culture (scale bar: 200 μm). (h) Quantification of cell alignment after 7 d of culture. Data in (c, d, f) are expressed as mean±standard deviation (n=3). ns: not significant

(Fig. 3c) further supported these findings, demonstrating comparable cell proliferation rates on both UCSFB and OCSFB over 7 d. Hemolysis assays (Figs. 3e and 3f) revealed hemolysis rates of <5% for both scaffold types, indicating good blood compatibility and suggesting suitability for in vivo applications. Phalloidin staining of the cytoskeleton (Fig. 3g) revealed a more elongated and aligned cell morphology on OCSFB than on UCSFB. Quantification (Fig. 3h) confirmed a significantly higher cell orientation along the unidirectional structure of OCSFB throughout the 7-d culture period. This organized cellular alignment, mimicking the native tendon architecture, was crucial for tendon repair and might improve tissue regeneration.

2.3 Collagen expression and mechanotransduction marker analysis on UCSFB and OCSFB

Immunofluorescence staining for COL1 and COL3 was performed to evaluate ECM production on UCSFB and OCSFB scaffolds. At Day 3 (Fig. 4a), COL1 and COL3 expression was relatively low on both scaffold types, with no significant intergroup differences. However, by Day 7 (Fig. 4c), OCSFB exhibited significantly higher COL1 and COL3 expression than UCSFB, as confirmed by quantitative fluorescence analysis (Figs. 4b and 4d), suggesting that the aligned structure of OCSFB provided a more favorable environment for ECM production, which is crucial for tendon repair. The increased collagen deposition on OCSFB may contribute to improved tissue regeneration and mechanical strength, thereby mimicking the native tendon matrix. To further explore the mechanotransduction pathways, we analyzed the expression of the mechanosensing regulators TAZ and YAP1 at Day 7. Immunofluorescence staining (Figs. 4f and 4g) revealed a higher expression of both TAZ and YAP1 in cells on OCSFB than on UCSFB. Quantitative analysis (Fig. 4e) confirmed significantly increased fluorescence intensity for both markers on OCSFB. These results indicate that the oriented microstructure of OCSFB improves mechanotransduction signaling, which may further promote cell alignment, proliferation, and ECM production.

2.4 Gene and protein expression analysis of tendon-related markers on UCSFB and OCSFB scaffolds

We analyzed the mRNA expression levels of key tendon-related genes, including *COL1A1*, *COL3A1*, *TNC*, and *TNMD*, by reverse transcription-polymerase chain reaction (RT-PCR) on Day 7 (Figs. 5a–5d). Cells cultured on OCSFB exhibited significantly higher expression of all four genes than cells cultured on UCSFB and the negative control (NC) group. Specifically, the expression of *COL1A1* and *COL3A1*, encoding *COL1* and *COL3*, respectively, was significantly upregulated in the OCSFB group (Figs. 5a and 5b), suggesting increased ECM production. Moreover, the expression of *TNC* and *TNMD*, which are critical for tendon development and repair, was significantly upregulated in the OCSFB group (Figs. 5c and 5d). Remarkably, this improved tenogenic response extended to key transcription factors and regulatory molecules that govern the specification of tendon lineage. Both the master tendon transcription factor scleraxis (Scx) and the tendon maturation regulator thrombospondin-4 (Thbs4) were significantly upregulated in cells on OCSFB compared with those on UCSFB (Fig. S1 in the supplementary information, $p<0.0001$). The simultaneous activation of both structural components (collagens) and regulatory factors (Scx and Thbs4) demonstrates that the aligned OCSFB architecture effectively enhances the tenogenic program at multiple molecular levels, probably by providing physical cues that mimic the native tendon niche. Western blotting was performed to evaluate the protein levels of COL1A2, COL3A1, and TNMD (Fig. 5e), which revealed that, consistent with the gene expression data, cells cultured on the OCSFB scaffold exhibited significantly higher protein levels than cells cultured on the UCSFB scaffolds and the NC group, as demonstrated by quantitative grayscale analysis (Figs. 5f–5h). The significant upregulation of COL1A2 and COL3A1 indicates increased collagen deposition, which is essential for tendon strength and function. Moreover, the elevated expression of TNMD, a marker of mature tenocytes, suggests that the OCSFB scaffold facilitates tendon maturation and repair.

2.5 Scaffold implantation and evaluation of tendon healing in a rat Achilles tendon injury model

The anti-adhesion and tendon-healing properties of UCSFB and OCSFB were evaluated using a rat Achilles tendon injury model with scaffold implantation. Both scaffolds were easily wrapped around the injured tendon and sutured in place. Histological analysis, using hematoxylin and eosin (H&E) and Masson's trichrome staining, was performed at 2- and 4-week postimplantation to evaluate tendon healing and adhesion formation in the blank, UCSFB, and OCSFB groups (Figs. 6b and 6c). The blank group, in which no scaffold was implanted, demonstrated severe adhesion formation and disorganized tendon structure, particularly at 4 weeks. In contrast, the OCSFB group showed reduced adhesion formation and a more organized tendon structure compared to the UCSFB and blank groups. At 2 weeks, the OCSFB group exhibited early signs of tendon regeneration, characterized by aligned collagen fibers and minimal adhesion formation. However, the UCSFB group exhibited moderate adhesions and a less organized tendon structure. By 4 weeks, the

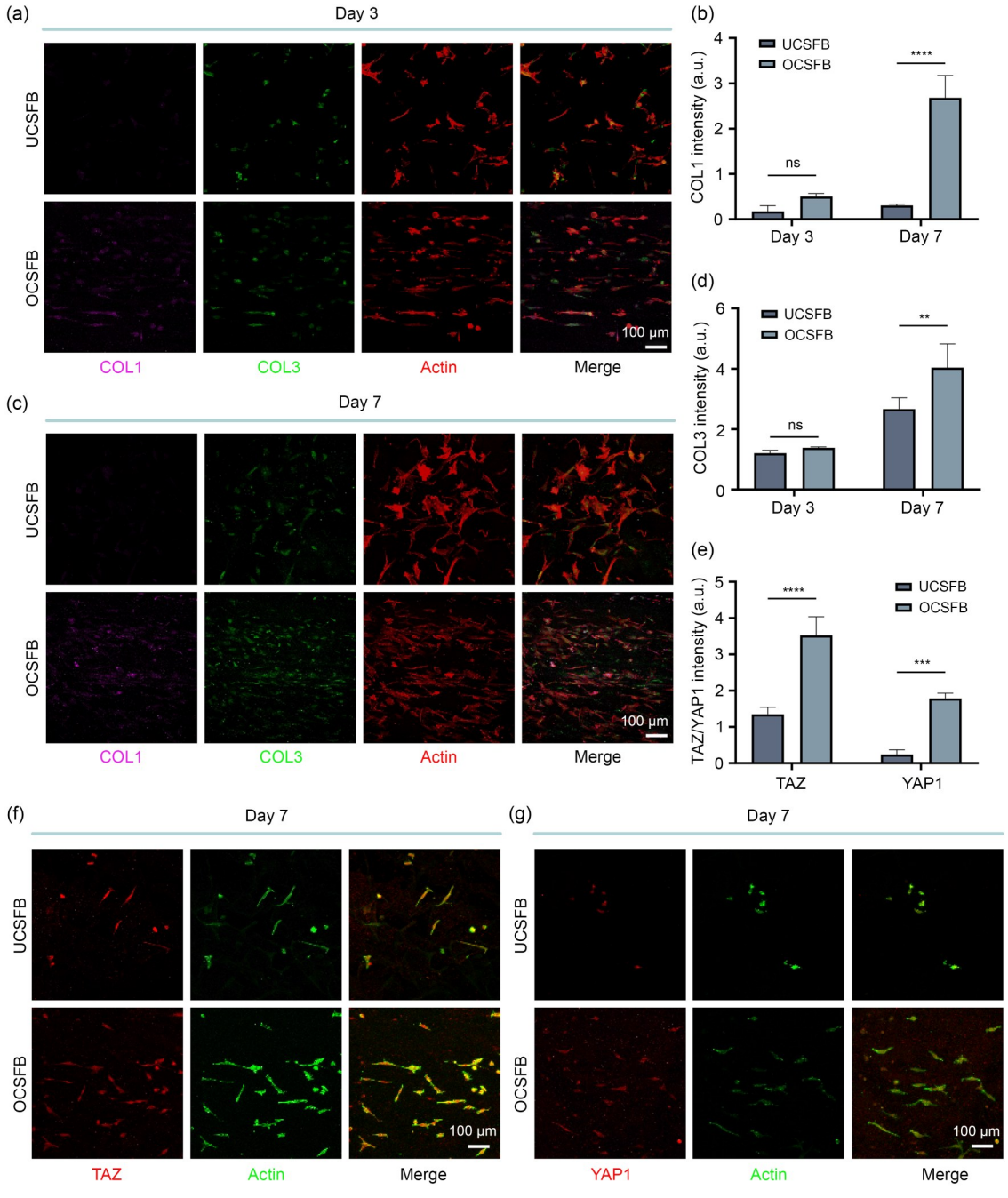

Fig. 4 Collagen expression and mechanotransduction marker analysis on UCSFB and OCSFB. (a) Immunofluorescence staining for COL1, COL3, and actin on the scaffolds at Day 3 (scale bar: 100 μm). (b) Quantitative analysis of COL1 fluorescence intensity at Days 3 and 7. (c) Immunofluorescence staining for COL1, COL3, and actin on the scaffolds at Day 7 (scale bar: 100 μm). (d) Quantitative analysis of COL3 fluorescence intensity at Days 3 and 7. (e) Quantitative analysis of TAZ and YAP1 fluorescence intensity at Day 7. (f) Immunofluorescence staining for TAZ and actin on the scaffolds at Day 7 (scale bar: 100 μm). (g) Immunofluorescence staining for YAP1 and actin on the scaffolds at Day 7 (scale bar: 100 μm). Data in (b, d, e) are expressed as mean±standard deviation (n=3). $^{**}p<0.01$, $^{***}p<0.001$, $^{****}p<0.0001$. ns: not significant

OCSFB group demonstrated further improvements in tendon healing, with dense, aligned collagen fibers and minimal adhesions, indicative of superior tendon regeneration. Masson's trichrome staining (Fig. 6c) was performed to evaluate collagen deposition and the extent of adhesion formation. In the blank group, excessive collagen deposition was evident at both 2 and 4 weeks, indicative of significant scar tissue formation and adhesions. The UCSFB group also displayed collagen deposition, although to a lesser extent than the blank group. In contrast, the OCSFB group demonstrated well-organized collagen fibers with minimal scar tissue, particularly at 4 weeks. The aligned structure of the OCSFB

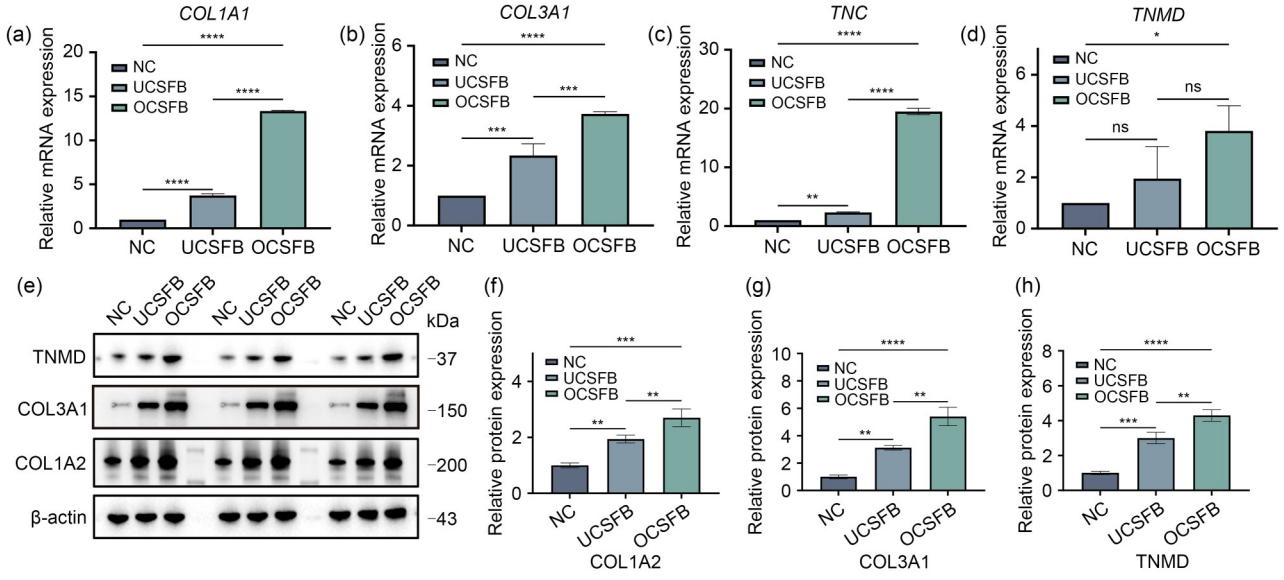

Fig. 5 Gene and protein expression of tendon-related markers in cells cultured on UCSFB and OCSFB. (a–d) RT-PCR analysis of *COL1A1* (a), *COL3A1* (b), *TNC* (c), and *TNMD* (d) mRNA expression levels in cells cultured on UCSFB and OCSFB scaffolds on Day 7. (e) Western blot analysis of COL1A2, COL3A1, and TNMD protein levels in cells cultured on UCSFB and OCSFB at Day 14 (β-actin served as a loading control). Quantification of COL1A2 (f), COL3A1 (g), and TNMD (h) protein levels based on western blot band grayscale intensity. Data in (a–d, f–h) are expressed as mean±standard deviation (n=3). $^{*}p<0.05$, $^{**}p<0.01$, $^{***}p<0.001$, $^{****}p<0.0001$. ns: not significant

scaffold probably facilitated appropriate collagen fiber alignment, which is essential for functional tendon regeneration and reducing adhesion formation. The Tang scoring system was used for quantitative scoring of adhesion formation on the tendon surface and inside the tendon (Figs. 6d and 6e), where lower scores represent less adhesion. At both 2 and 4 weeks, the OCSFB group showed significantly lower adhesion scores than the UCSFB and blank groups, indicating that the OCSFB scaffold effectively reduced adhesion formation. Furthermore, tendon healing was evaluated using the Soslowsky, Svensson, and Cook scoring system (Fig. 6f), where lower scores indicate better tendon healing. The OCSFB group exhibited the lowest pathological scores at both points, indicating that the OCSFB scaffold promoted superior tendon regeneration and prevented tendon adhesions. Furthermore, immunofluorescence staining of inflammatory markers at 2 and 4 weeks postsurgery provided additional insights into the healing process. Figures S4a–S4f (supplementary information) show the representative images of CD68, CD206, and MPO staining for the blank, UCSFB, and OCSFB groups. Quantification of positive areas for these markers revealed that the OCSFB group exhibited significantly lower infiltration of CD68-positive macrophages and MPO-positive neutrophils at both time points than the UCSFB and blank groups (Figs. S4g and S4i in the supplementary information). Moreover, a higher proportion of CD206-positive M2 macrophages was detected in the OCSFB group (Fig. S4h in the supplementary information), suggesting a favorable polarization toward an anti-inflammatory phenotype. These findings indicate that OCSFB not only facilitated tendon healing but also modulated the inflammatory response, which is essential for optimal tendon regeneration and for reducing adhesion formation.

2.6 Evaluation of collagen organization, COL1/COL3 ratio, and tendon-healing markers in the rat Achilles tendon injury model

The evaluation of collagen fiber organization using Sirius red staining under polarized light (Fig. 7a) revealed more organized and aligned collagen fibers in the OCSFB group than in the UCSFB and blank groups, particularly at 4 weeks. This result suggests improved collagen alignment with OCSFB, crucial for tendon function. The UCSFB group exhibited less organized fibers, whereas the blank group demonstrated the most disorganization. Quantitative analysis of the COL1/COL3 area ratio (Fig. 7b) and immunofluorescence staining (Fig. 7c) indicated a significantly higher COL1/COL3 ratio in the OCSFB group at both 2 and 4 weeks, signifying more mature collagen composition and reduced scar tissue formation than those in the UCSFB and blank groups. To further explore the mechanisms underlying this improvement, we investigated the expression of TNMD and YAP (Figs. 7e and 7f). Interestingly, the expression of YAP, a marker associated with mechanotransduction and fibrosis, also increased significantly in the OCSFB group. Notably, this concurrent upregulation of TNMD and YAP suggests that OCSFB affects the mechanotransduction and maturation processes during tendon healing.

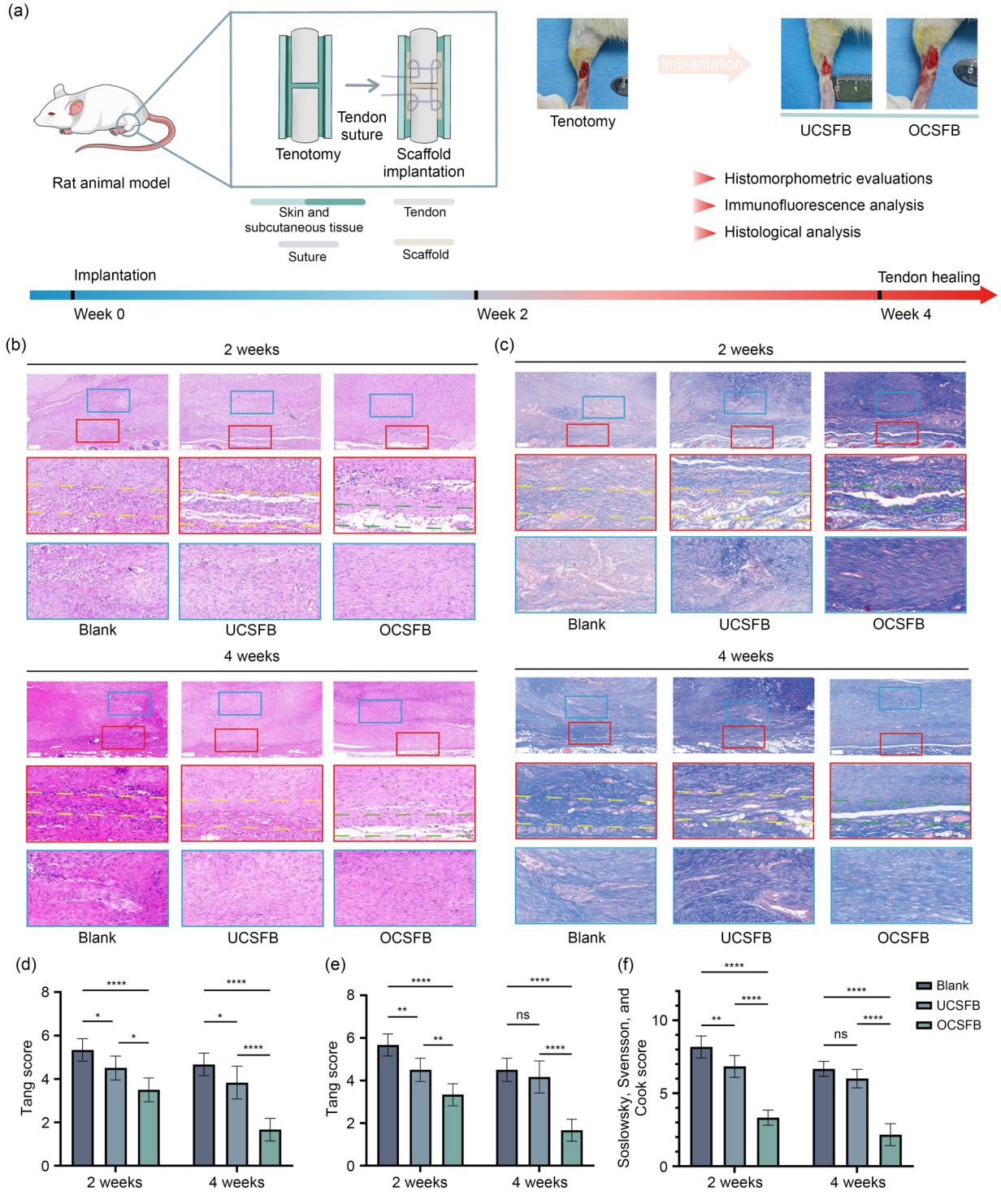

Fig. 6 Scaffold implantation and evaluation of tendon healing in a rat Achilles tendon injury model. (a) Schematic of the rat Achilles tendon injury model and scaffold implantation procedure. After tenotomy, UCSFB or OCSFB scaffolds were wrapped around the injured tendon and sutured in place. The timeline indicates scaffold implantation at week 0 and tendon-healing assessments at weeks 2 and 4, including histomorphometric evaluations, immunofluorescence analysis, and histological analysis. (b) H&E staining of tendon tissue at 2 and 4 weeks postimplantation in the blank, UCSFB, and OCSFB groups (scale bars: 200 μm). (c) Masson's trichrome staining of tendon tissue at 2 and 4 weeks postimplantation in the blank, UCSFB, and OCSFB groups (scale bars: 200 μm). Quantitative scoring of adhesion formation on the tendon surface (d) and inside the tendon (e) using the Tang scoring system (lower scores indicating less adhesion). (f) Tendon-healing scores at 2 and 4 weeks postimplantation based on the Soslowsky, Svensson, and Cook scoring system (lower scores indicating better tendon healing). Data are expressed as mean±standard deviation (n=3). Statistical significance was determined by one-way analysis of variance (ANOVA) with Tukey's post hoc test ($^{*}p<0.05$, $^{**}p<0.01$, $^{****}p<0.0001$; ns: not significant)

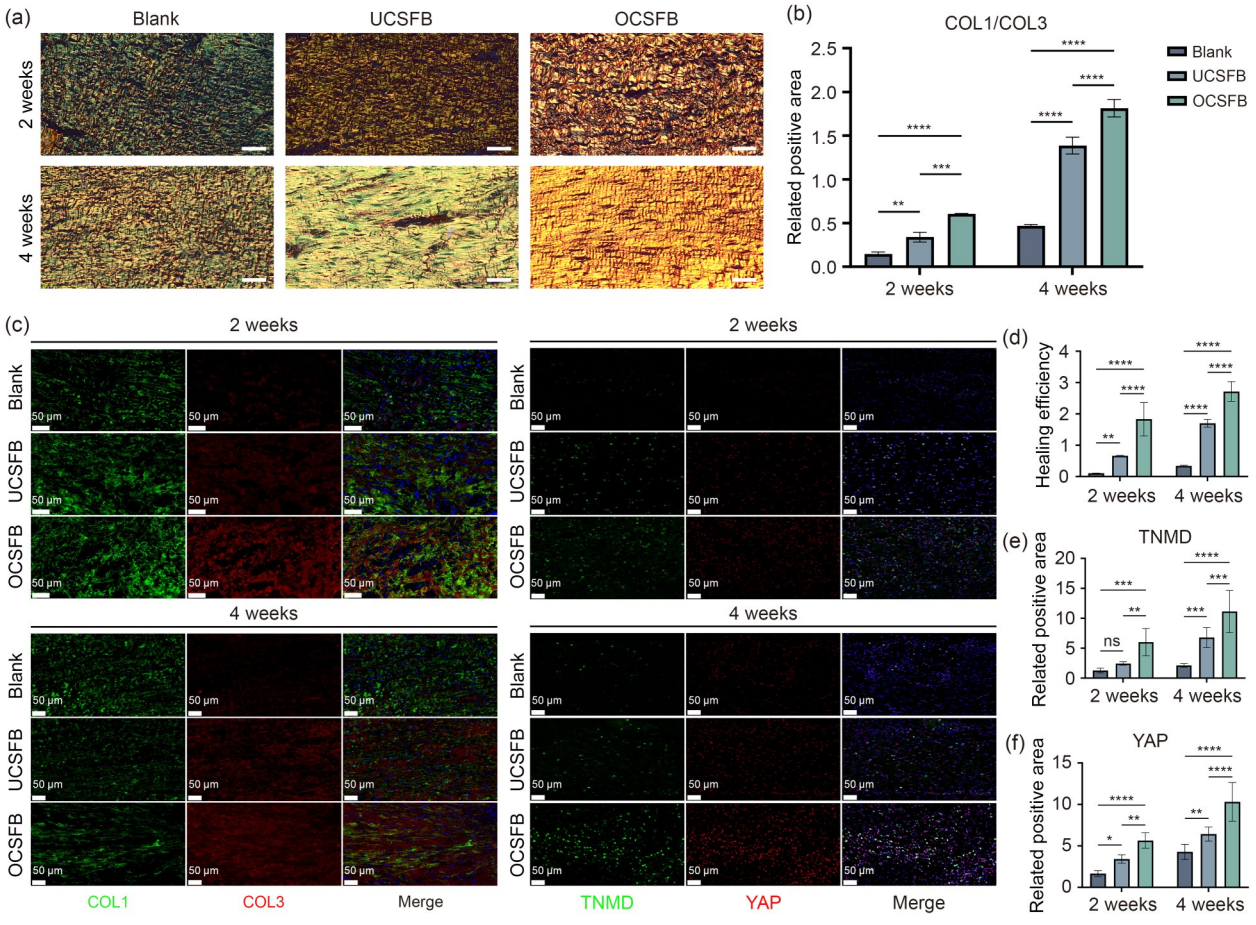

Fig. 7 Evaluation of collagen organization, COL1/COL3 ratio, and tendon-healing markers in the rat Achilles tendon injury model. (a) Representative images of Sirius red staining under polarized light showing collagen fiber organization at 2 and 4 weeks postsurgery (blank, UCSFB, and OCSFB). Scale bars: 50 μm. (b) Quantification of COL1/COL3 area ratio from Sirius red staining (2 and 4 weeks). (c) Representative immunofluorescence images of COL1 (green), COL3 (red), TNMD (green), YAP (red), and nuclei (DAPI, blue) at 2 and 4 weeks. (d) Tendon-healing efficiency at 2 and 4 weeks. (e) TNMD expression quantified by immunofluorescence staining (2 and 4 weeks). (f) YAP expression quantified by immunofluorescence staining (2 and 4 weeks). Data are expressed as mean±standard deviation (n=3). One-way analysis of variance (ANOVA) with Tukey's post hoc test was used for statistical analysis ($^{*}p<0.05$, $^{**}p<0.01$, $^{***}p<0.001$, $^{****}p<0.0001$; ns: not significant). DAPI: 4',6-diamidino-2-phenylindole

2.7 Gait analysis and mechanical strength assessment of repaired Achilles tendons

Gait analysis and mechanical testing were conducted to evaluate the functional recovery and mechanical strength of repaired Achilles tendons. Gait analysis was conducted at 7, 14, and 28 d postimplantation using the Achilles functional index (AFI) (Figs. 8a–8c). Footprint analysis (Fig. 8b) revealed progressive normalization of gait in the OCSFB group compared to the UCSFB and blank groups, approaching the gait pattern of the native group by 14 and 28 d. The AFI scores (Fig. 8c) corroborated these observations, with the OCSFB group demonstrating significantly improved functional recovery at all time points. The UCSFB group exhibited moderate improvement, whereas the blank group showed minimal recovery. Mechanical testing was performed at 4 weeks postimplantation (Figs. 8d–8g), in which the OCSFB group exhibited a significantly higher tensile modulus (Figs. 8f and 8g), indicating improved tendon regeneration and increased resistance to deformation under load. The stress–strain curves (Fig. 8e) further confirmed the superior mechanical properties of OCSFB. The UCSFB group demonstrated moderate mechanical strength, whereas the blank group showed the weakest properties.

2.8 RNA-seq analysis of differential gene expression between the blank, UCSFB, and OCSFB groups

The gene expression profiles of tendon tissues (n=3 per group) were evaluated at 4 weeks postsurgery by RNA-seq in the blank, UCSFB, and OCSFB groups. Principal component analysis (PCA) showed that PC1 accounted for 76.01% of the total variance, distinctly separating the OCSFB group from the blank and UCSFB groups along PC1 (Fig. 9a). Sample correlation analysis (Fig. 9b) confirmed high consistency

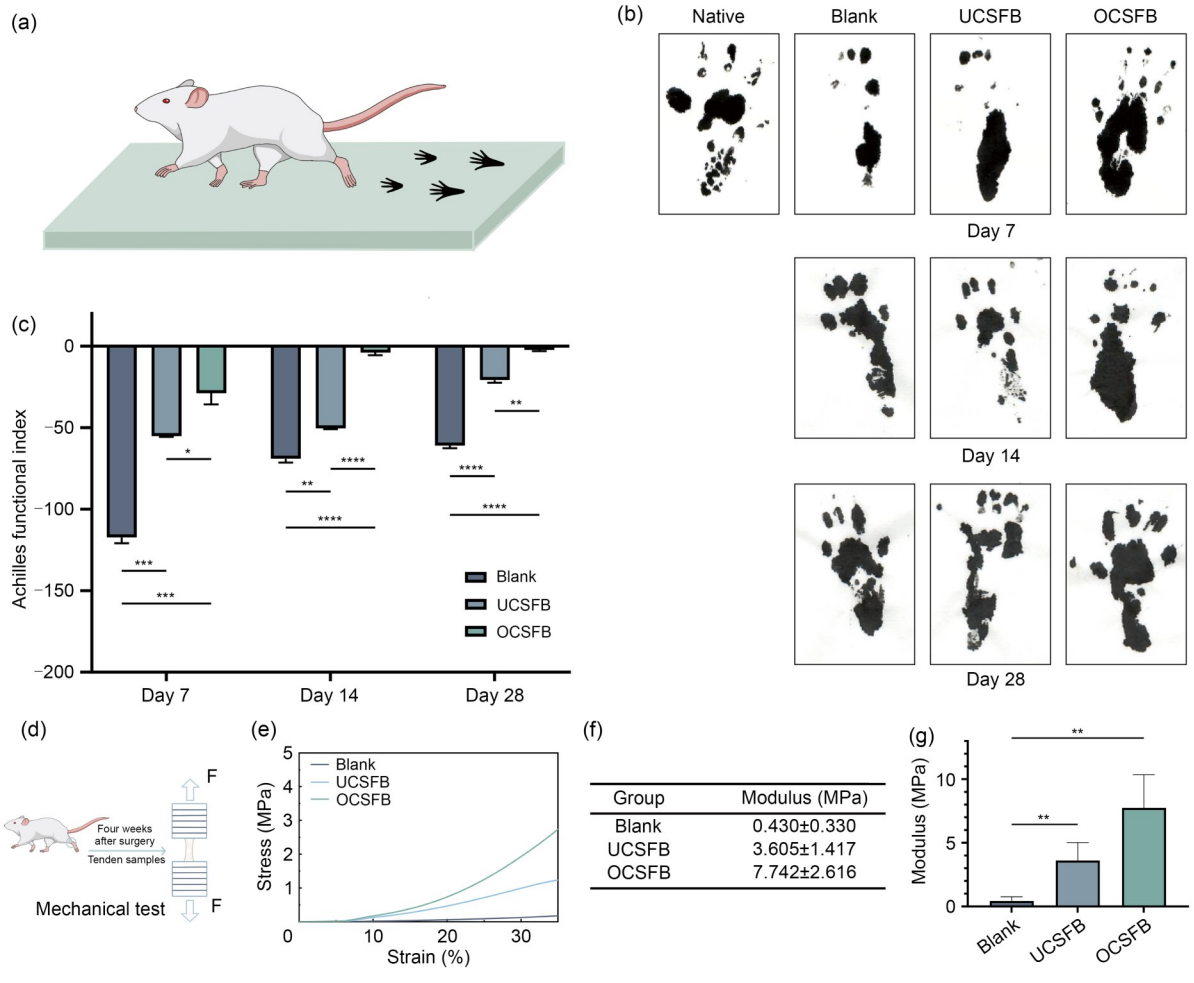

Fig. 8 Functional and mechanical analysis of repaired Achilles tendons. (a) Schematic of the gait analysis setup. (b) Representative footprint images at 7, 14, and 28 d (native, blank, UCSFB, and OCSFB). (c) Achilles functional index (AFI) scores at 7, 14, and 28 d. (d) Schematic of the mechanical testing setup (4 weeks). (e) Stress–strain curves (4 weeks). (f) Tensile modulus values at 4 weeks. (g) Quantification of tensile modulus (4 weeks). Data are expressed as mean±standard deviation (n=3). One-way analysis of variance (ANOVA) with Tukey's post hoc test was used for statistical analysis ($^{*}p<0.05$, $^{**}p<0.01$, $^{***}p<0.001$, $^{****}p<0.0001$)

within each group, indicating reliable data quality. DESeq2 analysis identified differentially expressed genes (padj<0.05, $|\log_2 \text{FoldChange}|>1$). In the OCSFB vs. blank comparison, 2206 genes were upregulated and 1639 were downregulated. In the UCSFB vs. blank comparison, 257 genes were upregulated and 519 were downregulated. The OCSFB vs. UCSFB comparison revealed 2538 upregulated and 1475 downregulated genes (Figs. 9d–9f). Heatmap analysis (Fig. 9c) highlighted substantial differences in gene expression patterns, particularly in the OCSFB group. Kyoto Encyclopedia of Genes and Genomes (KEGG) analysis revealed an enriched CAM pathway in the OCSFB group (Figs. 9g – 9i). This result suggests that OCSFB treatment modulates cell–matrix interactions, potentially reducing adhesion formation and promoting tissue repair. OCSFB treatment probably promotes cell migration and tissue regeneration by modulating the expression of key adhesion molecules, such as integrins, cadherins, and members of the immunoglobulin superfamily (IgSF CAMs). This modulation may contribute to the reduction of excessive adhesion formation. OCSFB treatment also significantly affected the expression of integrins and cadherins, which are essential for cell adhesion and migration. These molecules facilitate interactions between cells and the ECM, thereby improving tissue integrity and regenerative capacity. OCSFB treatment may also downregulate certain adhesion molecules associated with inflammatory responses, such as intercellular adhesion molecule 1 (ICAM1) and vascular cell adhesion molecule 1 (VCAM1), potentially mitigating excessive inflammation and fibrosis, which are known contributors to adhesion formation. To summarize, RNA-seq analysis and KEGG enrichment results indicate that OCSFB treatment modulates the CAM pathway, promoting tissue repair and potentially reducing adhesion formation. These results emphasize the potential of OCSFB as a therapeutic strategy for improving tissue regeneration and preventing adhesions.

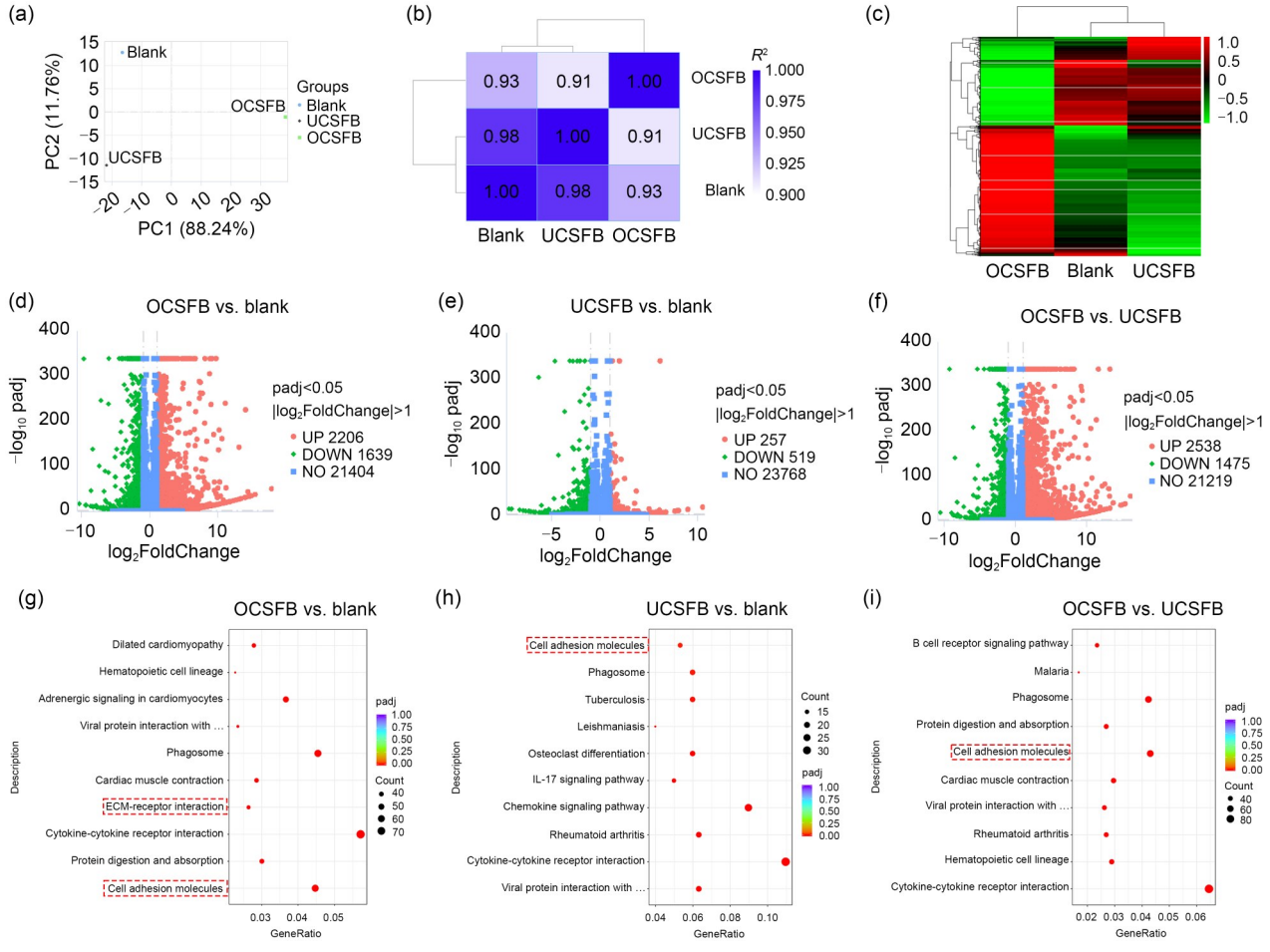

Fig. 9 RNA-seq analysis of gene expression changes induced by OCSFB. (a) PCA plot. (b) Sample correlation heatmap. (c) Heatmap presenting the normalized expression levels of differentially expressed genes across groups. Values are expressed as z-scores (dimensionless), with red indicating higher expression and green indicating lower expression relative to the mean expression level. (d–f) Volcano plots of differentially expressed genes for OCSFB vs. blank, UCSFB vs. blank, and OCSFB vs. UCSFB. (g–i) KEGG pathway enrichment analysis for OCSFB vs. blank, UCSFB vs. blank, and OCSFB vs. UCSFB

3 Discussion

We developed OCSFBs and demonstrated their effectiveness in improving tendon repair by combining physical barrier properties with the promotion of intrinsic healing. The OCSFB fabricated by directional freeze-casting possesses unidirectionally aligned microfibers that mimic the native tendon architecture [28–31], providing both structural support and biological cues for tendon regeneration.

Our results confirmed that OCSFB acted as an effective physical barrier, preventing the infiltration of the surrounding fibrous tissues into the healing site and thereby reducing adhesion formation. In vivo experiments demonstrated that tendons treated with OCSFB exhibited significantly fewer adhesions than those treated with UCSFB or left untreated (Figs. 6d and 6e). Histological analyses further confirmed minimal adhesion tissue in the OCSFB group, emphasizing the efficacy of the scaffold. The barrier function was further validated by Transwell migration assays, which demonstrated that OCSFB completely blocked the migration of macrophages, thus confirming its ability to prevent external cellular infiltration.

The aligned structure of OCSFB promoted intrinsic tendon healing by providing topographical cues that guided cellular behavior and improved mechanotransduction pathways [14, 32–36]. In vitro experiments revealed that cells cultured on OCSFB exhibited improved alignment and elongation along the direction of the microfibers, facilitating the orderly deposition of ECM components, particularly COL1 and COL3, which are essential for tendon strength and functionality [37–41]. The topography of the scaffold influenced cytoskeletal organization and might activate mechanosensing signaling pathways, thereby stimulating cellular activities crucial for tissue repair [42–45]. Furthermore, we observed an upregulation of tendon-specific genes and proteins, such as TNC and TNMD, and RNA-seq analysis revealed modulation of genes involved in the CAM pathway. These observations indicate that OCSFB promoted tendon maturation

and regeneration by facilitating beneficial cell–matrix and cell–cell interactions and inhibiting processes that result in fibrosis and adhesion formation.

Our finding of increased YAP expression in the OCSFB group initially appeared contradictory to the observed anti-adhesion effects, because YAP is often associated with fibrosis. Nevertheless, in tendon-specific contexts, YAP signaling plays a nuanced role that depends critically on microenvironmental cues. Tao et al. demonstrated that activating YAP through LncRNA H19 improved the proliferation, migration, and differentiation of tendon stem cells, significantly improving tendon healing [46]. The aligned microstructure of OCSFB probably provided optimal mechanical signals that direct YAP activity toward tendon-specific regeneration pathways, as evidenced by the concurrent upregulation of TNMD. Remarkably, Lu et al. reported that loading platelet-derived exosomes with recombinant Yap1 improved the stemness and differentiation of tendon stem/progenitor cells (TSPCs), promoting functional tendon regeneration in a full-cut Achilles tendon defect model [47]. These data suggest that in the appropriate context, YAP activation promotes ordered tissue repair rather than pathological fibrosis. Crucially, the barrier function of OCSFB may further contribute by confining YAP activity to intrinsic tendon cells and preventing the infiltration of external fibroblasts that could otherwise contribute to adhesive scarring.

In vivo implantation of OCSFB in a rat Achilles tendon injury model confirmed its dual functionality of reducing adhesions and promoting organized tissue regeneration. Tendons treated with OCSFB exhibited organized collagen fiber alignment resembling the healthy tendon tissue. Consequently, immunofluorescence staining revealed reduced infiltration of CD68-positive macrophages and MPO-positive neutrophils in the OCSFB group, along with increased infiltration of CD206-positive M2 macrophages, indicating a modulated inflammatory response that supports regeneration rather than fibrosis. Functional assessments, including gait analysis and mechanical testing, demonstrated that OCSFB-treated tendons regained normal functionality more rapidly and possessed greater tensile strength than control tendons. These data indicate that the OCSFB effectively restored both the structural and functional integrity of injured tendons.

Our study demonstrated that OCSFB represents a promising strategy for tendon repair by combining physical barrier properties with the promotion of intrinsic healing through structural alignment. By preventing adhesion formation and guiding organized tissue regeneration, OCSFB addresses two major challenges in tendon healing. Compared to existing anti-adhesion barriers that often provide only passive separation, OCSFB actively promotes healing and prevents adhesions. Nevertheless, our study has certain limitations, including the relatively short-term follow-up period and the use of a single animal model. Future studies should focus on optimizing scaffold properties, investigating long-term efficacy, and evaluating their potential in clinical applications to completely realize their therapeutic benefits.

4 Conclusions

This study demonstrates the development and efficacy of an OCSFB scaffold for preventing tendon adhesions and improving healing. OCSFB, fabricated via directional freeze-casting, combines the biocompatibility of SF with an aligned microstructure that mimics native tendon architecture. In vitro analyses demonstrated that OCSFB promotes cell alignment and upregulates tendon-specific genes and proteins, while enhancing mechanotransduction pathways crucial for tendon regeneration. In a rat Achilles tendon model, OCSFB significantly reduced adhesion formation and promoted organized tissue regeneration, with histological analyses confirming minimal adhesions along with well-organized collagen alignment. Functional evaluations demonstrated faster recovery of normal gait and superior mechanical strength in OCSFB-treated tendons. RNA-seq revealed that OCSFB modulates the CAM pathway, providing mechanistic insights into its dual functionality as a physical barrier and a promoter of intrinsic healing. The ability of OCSFB to simultaneously prevent adhesions and promote functional regeneration represents a significant advancement over existing strategies that typically provide only passive separation. These findings establish OCSFB as a promising therapeutic strategy for tendon injury management, addressing the critical balance between adhesion prevention and functional tissue repair.

5 Methods

5.1 Bandage fabrication

5.1.1 Preparation of SF solution

SF powder (EFL-SF-001, Yongqinquan Intelligent Equipment Co., Ltd., China) was dissolved in deionized water to prepare solutions at concentrations of 2%, 4%, 6%, and 10% (mass fraction). The mixtures were stirred gently until the SF completely dissolved. Dissolved air was removed from the resulting SF solutions by vacuum degassing before subsequent processing.

5.1.2 OCSFB fabrication

OCSFBs were fabricated using a directional freeze-casting technique. The SF solutions were poured into custom-designed molds fabricated by fused deposition modeling

(FDM) 3D printing (Bambu Lab, China). The molds were placed on a copper cold finger maintained at −90 °C using liquid nitrogen. This controlled directional freeze-casting process yielded bandages with an oriented microporous structure.

5.1.3 UCSFB fabrication

UCSFBs were fabricated for comparison. A 2% SF solution was poured into the same molds and frozen at −20 °C for 12 h in a conventional freezer. This uncontrolled freezing process resulted in a random, microporous structure.

5.1.4 Freeze-drying and annealing

After freezing, all samples were freeze-dried using a lyophilizer at −76 °C and 10 Pa for 48 h to remove any remaining solvent. The dried bandages were then subjected to water annealing at room temperature (95% relative humidity) for 20 min. Water vapor for annealing was generated by heating water to 60 °C, which facilitated the stabilization of the SF structure.

5.1.5 Compression and crosslinking

After annealing, all samples were compressed at 5 MPa for 10 min, perpendicular to the freezing direction, to improve their mechanical properties. In contrast to the OCSFBs, the UCSFB samples were compressed along their longitudinal axis. After compression, all samples were immersed in 95% ethanol for 24 h to induce crosslinking of SF. The samples were then washed three times with deionized water to remove residual ethanol.

5.1.6 Storage

After the completion of crosslinking, the bandages were stored in 75% ethanol at room temperature until further use in experiments.

5.2 Small-angle X-ray scattering

The orientation and nanoscale structure of the SF scaffolds were analyzed by SAXS (XEUSS 3.0, XENOCS, France). The X-ray wavelength was 0.135 nm, and the sample-to-detector distance was set to 1000 mm. SAXS was performed to compare the degree of orientation between 2% OCSFB and 2% UCSFB. The scattering data were processed to quantify the alignment of the nanostructures in both types of scaffolds.

5.3 Crystallinity and bond characterization

To examine the crystallinity and molecular structure of the SF scaffolds, the samples were divided into four groups as follows: 2% OCSFB crosslinked, 2% OCSFB uncrosslinked, 2% UCSFB crosslinked, and 2% UCSFB uncrosslinked. The following techniques were used:

WAXS (XEUSS 3.0, XENOCS) was used to evaluate the crystalline structure and β-sheet content. The sample-to-detector distance was set to 42.5 mm.

XRD (Bruker D8 Advance, Bruker, Germany) was used to characterize the crystalline phases and quantify the degree of crystallinity.

TGA (Mettler-Toledo, China) was used to measure the thermal stability and decomposition profiles by monitoring the weight loss as a function of temperature.

DSC (DSCQ1000, TA Instruments, USA) was used to measure thermal transitions, including the glass transition temperature (T_g) and melting temperature (T_m), to evaluate the thermal behavior before and after crosslinking.

FTIR spectroscopy. The chemical composition and secondary structure of the SF scaffolds were analyzed by ATR-FTIR spectroscopy (Nicolet iS50, Thermo Fisher, China). FTIR spectra were collected to evaluate the molecular structures and confirm the presence of characteristic secondary structures, such as α-helices and β-sheets, across all four groups, viz., 2% OCSFB crosslinked, 2% OCSFB uncrosslinked, 2% UCSFB crosslinked, and 2% UCSFB uncrosslinked.

5.4 Scanning electron microscopy

The microstructure of the SF composites was characterized using a thermal field emission scanning electron microscope (GeminiSEM 300 and GeminiSEM 200, Zeiss, Germany) equipped with EDS.

5.5 Mechanical testing

Mechanical properties were evaluated using a universal testing machine (UTM2102, Shenzhen Suns Technology Stock Co., Ltd., China) at a tensile speed of 5 mm/min.

5.6 Cell viability and proliferation assay

Rat tendon-derived stem/progenitor cells were isolated and cultured in Dulbecco's modified Eagle medium (KeyGEN, China) supplemented with 10% fetal bovine serum (Transgen, China) and 1% penicillin–streptomycin (KeyGEN). The cells were seeded onto the OCSFB and UCSFB scaffolds at a density of 1×10^5 cells per scaffold. Cell viability was evaluated using a live/dead staining kit (KeyGEN) at 1, 3, 5, and 7 d. Live cells were stained with Calcein-AM, and dead cells were stained with ethidium homodimer-1. Viable and nonviable cells were observed and quantified under an inverted fluorescence microscope (Mshot, China). Cell proliferation was quantified using the CCK-8 (KeyGEN) at the

same time points. Absorbance was measured at 450 nm using a microplate reader to evaluate the metabolic activity of cells, correlating with cell proliferation. Cell morphology and alignment were analyzed by staining the actin cytoskeleton with phalloidin (Beyotime, China) and counterstaining the nuclei with 4',6-diamidino-2-phenylindole (DAPI; Thermo Fisher Scientific, USA). However, during imaging, the SF scaffolds exhibited strong autofluorescence, particularly in the ultraviolet and blue spectral ranges, overlapping with the emission spectrum of DAPI. This autofluorescence masked the DAPI signal, hindering the visualization of the stained cell nuclei. Furthermore, there was nonspecific adsorption of DAPI onto the silk scaffolds, further complicating the interpretation of the DAPI channel. Consequently, the DAPI channel was excluded from the final images, and the analysis focused on actin cytoskeleton staining to evaluate cell alignment on the OCSFB and UCSFB scaffolds. Fluorescence images were acquired using a confocal microscope (Zeiss).

5.7 Immunofluorescence staining

Samples were fixed in 4% paraformaldehyde (PFA) for 10 min and washed three times with phosphate-buffered saline (PBS). Permeabilization was performed with 0.1% Triton X-100 for 10 min, followed by blocking in 1% bovine serum albumin (BSA) for 30 min. The samples were then incubated with primary antibodies overnight at 4 °C. After three washes with PBS, the corresponding secondary antibodies were applied for 1 h at room temperature. Finally, nuclei were counterstained with DAPI for 5 min. Images were acquired using a Zeiss LSM 880 confocal microscope.

5.8 RNA isolation and qPCR

Total RNA was extracted from cells cultured on the OCSFB and UCSFB scaffolds using FreeZol reagent (Vazyme, China), according to the manufacturer's protocol. RNA was reverse-transcribed into cDNA using a reverse transcription kit (Applied Biological Materials Inc., Canada). Quantitative reverse transcription PCR (qRT-PCR) was performed using 2× qPCR master mix (Applied Biological Materials Inc.) on a QuantStudio^{TM} 7 Pro real-time PCR system (Thermo Fisher, USA). The expression levels of tendon-related genes, including *COL1A1*, *COL3A1*, *TNC*, and *TNMD*, were evaluated, with *GAPDH* used as the internal control. Relative gene expression was calculated using the $2^{-\Delta\Delta C_t}$ method. All qRT-PCR assays were performed in triplicate to ensure experimental reproducibility.

5.9 Western blotting

The protein expression of COL1A2, COL3A1, and TNMD was evaluated by western blotting. Cells were lysed in radioimmunoprecipitation assay (RIPA) buffer containing protease inhibitors, and protein concentrations were measured using a bicinchoninic acid (BCA) protein assay kit (Thermo Fisher Scientific). Equal amounts of protein were separated by sodium dodecyl sulfate–polyacrylamide gel electrophoresis (SDS-PAGE) and transferred to polyvinylidene fluoride (PVDF) membranes. The membranes were blocked with 5% bovine serum albumin (BSA) and incubated overnight at 4 °C with primary antibodies. After washing, the membranes were incubated with horseradish peroxidase (HRP)-conjugated secondary antibodies and visualized using an enhanced chemiluminescence (ECL) substrate (Thermo Fisher Scientific). Band intensities were quantified by gray-scale analysis using ImageJ.

5.10 Animal model

Female Sprague–Dawley rats, aged 8–10 weeks and weighing 180–200 g, were used to establish an Achilles tendon injury model. The rats were housed under standard conditions, including a 12-h light/dark cycle, with free access to water and standard chow. General anesthesia was induced and maintained using isoflurane (4% for induction and 2% for maintenance in oxygen). A midline skin incision was made on the posterior aspect of the hindlimb to expose the Achilles tendon, followed by a full-thickness transverse transection at the midpoint of the tendon. In the blank group, the tendon was sutured using a modified Kessler suture technique without the application of a scaffold. In the scaffold groups, either UCSFB or OCSFB scaffolds were applied around the sutured tendon and secured with 6-0 nonabsorbable sutures. Incisions were closed layer by layer, and rats were allowed to recover with unrestricted movement.

5.11 Histological and immunofluorescence staining

Animals were randomly divided into three groups (n=6 per group/time point), i.e., blank (control), UCSFB, and OCSFB. Tendon samples were collected at 2 and 4 weeks postsurgery, fixed in 4% PFA, embedded in paraffin, and sectioned at 5-μm thickness. Sections were then stained with H&E for evaluating tissue morphology and adhesion formation, and with Masson's trichrome for evaluating collagen deposition. Sirius red staining under polarized light was performed to evaluate the organization of collagen fibers. Adhesion formation was quantified using the Tang scoring system, and tendon healing was scored using the Soslowsky, Svensson, and Cook system. For immunofluorescence staining, sections were deparaffinized and rehydrated, followed by antigen retrieval. Permeabilization was performed with 0.1% Triton X-100, followed by blocking with 1% BSA. Sections were incubated with primary antibodies overnight at 4 °C, washed, and then incubated with fluorescent secondary antibodies

for 1 h at room temperature. Nuclei were counterstained with DAPI. Sections were mounted with antifade mounting medium and imaged using a confocal microscope.

5.12 Gait analysis

Gait analysis was performed at 7, 14, and 28 d postsurgery to evaluate the functional recovery of the Achilles tendon. Footprints were collected, and the AFI was calculated. A higher AFI score indicates better functional recovery. At 4 weeks postsurgery, the mechanical properties of the repaired tendons were evaluated by tensile testing. Tendons were subjected to uniaxial tensile loading to determine the tensile modulus. Stress–strain curves were generated to evaluate tendon strength and resistance to deformation.

5.13 RNA-seq analysis

Tendon tissues were collected from the blank, UCSFB, and OCSFB groups at 4 weeks postsurgery (n=3 biological replicates per group) for RNA-seq analysis. Total RNA was extracted using the RNeasy Mini Kit (Qiagen, Germany), and sequencing libraries were prepared using the NEBNext Ultra RNA Library Prep Kit (New England Biolabs, USA). Sequencing was conducted on an Illumina NovaSeq 6000 platform (Illumina, USA) with 150 base pairs (bp) paired-end reads. Raw reads were quality-checked using FastQC and aligned to the rat reference genome (Rnor_6.0) with the spliced transcripts alignment to a reference (STAR) aligner. Differential expression analysis was performed using DESeq2, applying thresholds of adjusted p value (padj) <0.05 and $|\log_2\text{FoldChange}| > 1$ to identify significantly differentially expressed genes. KEGG pathway enrichment analysis was conducted on differentially expressed genes using the clusterProfiler R package to explore enriched biological pathways. Differential expression was determined using the DESeq2 pipeline, with statistical significance defined as adjusted p value (padj) <0.05 and $|\log_2\text{FoldChange}| > 1$.

5.14 Statistical analysis

All quantitative data, except RNA-seq results, are presented as mean±standard deviation. Statistical comparisons were performed using one-way analysis of variance (ANOVA) followed by Tukey's post-hoc test for multiple comparisons. A p-value <0.05 was considered statistically significant.

Supplementary Information The online version contains supplementary material available at https://doi.org/10.1631/bdm.2400495.

Acknowledgements This work was sponsored by the National Natural Science Foundation of China (Nos. 52235007, T2121004, and 52325504), the Key R&D Program of Zhejiang (No. 2024SSYS0027), the National Key Research and Development Program of China (Nos. 2024YFB4607700 and 2024YFB4607703), the China National Postdoctoral Program for Innovative Talents (No. BX20240312), and Dr. Li Dak Sum & Yip Yio Chin Development Fund for Regenerative Medicine, Zhejiang University.

Author contributions All authors made significant contributions to this work. PCX, GFL, and THQ contributed equally to the research design, data collection, and analysis. KY and CFH participated in experimental execution and data analysis. YH provided support in experimental design and supervision. JCG and YS, as corresponding authors, were responsible for research conceptualization, funding acquisition, supervision, and manuscript writing and revision.

Declarations

Conflict of interest YH is an associate editor for *Bio-Design and Manufacturing* and was not involved in the editorial review or the decision to publish this article. The authors declare that they have no conflict of interest.

Ethical approval All animal-related experiments in this study followed the National Institutes of Health (NIH) Guide for the Care and Use of Laboratory Animals and were approved by the Ethics Committee of Nanjing First Hospital of Nanjing Medical University (Approval No. DWSY-24054010).

Data availability All data generated or analyzed during this study are included in this published article.

References

1. Liu CJ, Bai JB, Yu KL et al (2019) Biological amnion prevents flexor tendon adhesion in zone II: a controlled, multicentre clinical trial. J BioMed Res Int 2019(1):2354325. https://doi.org/10.1155/2019/2354325
2. Tao MH, Liang F, He J et al (2021) Decellularized tendon matrix membranes prevent post-surgical tendon adhesion and promote functional repair. Acta Biomater 134:160–176. https://doi.org/10.1016/j.actbio.2021.07.038
3. Zhang XS, Xiao Y, Hu B et al (2024) Multi-omics analysis of human tendon adhesion reveals that ACKR1-regulated macrophage migration is involved in regeneration. Bone Res 12(1):27. https://doi.org/10.1038/s41413-024-00324-w
4. Hsu CH, Chen PY, Yang CP et al (2024) The results of preventing postoperative achilles tendon adhesion using cross-linked and non-cross-linked hyaluronic acid, a study with rat model. J Orthop Surg Res 19(1):457. https://doi.org/10.1186/s13018-024-04952-0
5. Liu S, Kang QL, Zhang R et al (2023) Tendon adhesion and novel solutions. In: Rosenberg N (Ed.), Trauma, Inflammation, Degeneration, and Treatment (1st Ed.). IntechOpen, p.108019. https://doi.org/10.5772/intechopen.108019
6. Leong NL, Kator JL, Clemens TL et al (2020) Tendon and ligament healing and current approaches to tendon and ligament regeneration. J Orthop Res 38(1):7–12. https://doi.org/10.1002/jor.24475
7. Maffulli N, Cuozzo F, Migliorini F et al (2023) The tendon unit: biochemical, biomechanical, hormonal influences. J Orthop Surg Res 18(1):311. https://doi.org/10.1186/s13018-023-03796-4
8. de Aro AA, de Campos Vidal B, Pimentel ER (2012) Biochemical and anisotropical properties of tendons. Micron 43(2–3):205–214. https://doi.org/10.1016/j.micron.2011.07.015
9. Hou JY, Yang R, Vuong I et al (2021) Biomaterials strategies to balance inflammation and tenogenesis for tendon repair. Acta

Biomater 130:1–16.
https://doi.org/10.1016/j.actbio.2021.05.043
10. Wang XC, Liu ZT, Sandoval-Salaiza DA et al (2021) Nanostructured non-Newtonian drug delivery barrier prevents postoperative intrapericardial adhesions. ACS Appl Mater Interfaces 13(25):29231–29246.
https://doi.org/10.1021/acsami.0c20084
11. Matar DY, Ng B, Darwish O et al (2023) Skin inflammation with a focus on wound healing. Adv Wound Care 12(5):269–287.
https://doi.org/10.1089/wound.2021.0126
12. Huang ST, Rao Y, Zhou M et al (2024) Engineering an extracellular matrix-functionalized, load-bearing tendon substitute for effective repair of large-to-massive tendon defects. Bioact Mater 36:221–237.
https://doi.org/10.1016/j.bioactmat.2024.02.032
13. Yin HY, Ding YF, Yan HG et al (2024) The essential role of aligned architecture in decellularized tendon matrix mediated stem cell tenogenic differentiation and tendon repair. Polym Test 132:108378.
https://doi.org/10.1016/j.polymertesting.2024.108378
14. Li SH, Sun Y, Chen YZ et al (2023) Sandwich biomimetic scaffold based tendon stem/progenitor cell alignment in a 3D microenvironment for functional tendon regeneration. ACS Appl Mater Interfaces 15(3):4652–4667.
https://doi.org/10.1021/acsami.2c16584
15. Wang K, Chen DY, Wang ZY et al (2023) An injectable and antifouling supramolecular polymer hydrogel with microenvironment-regulatory function to prevent peritendinous adhesion and promote tendon repair. Macromol Biosci 23(10):2300142.
https://doi.org/10.1002/mabi.202300142
16. Xue YM, Kim HJ, Lee JM et al (2022) Co-electrospun silk fibroin and gelatin methacryloyl sheet seeded with mesenchymal stem cells for tendon regeneration. Small 18(21):2107714.
https://doi.org/10.1002/smll.202107714
17. Lawrence BD, Infanger DW (2024) Effect of silk fibroin protein hydrolysis on biochemistry, gelation kinetics, and NF-kB bioactivity in vitro. Int J Biol Macromol 272:132702.
https://doi.org/10.1016/j.ijbiomac.2024.132702
18. Font Tellado S, Bonani W, Balmayor ER et al (2017) Fabrication and characterization of biphasic silk fibroin scaffolds for tendon/ligament-to-bone tissue engineering. Tissue Eng Part A 23(15–16):859–872.
https://doi.org/10.1089/ten.TEA.2016.0460
19. Lu K, Tang H, Wang Y et al (2023) Micropattern silk fibroin film facilitates tendon repair in vivo and promotes tenogenic differentiation of tendon stem/progenitor cells through the $\alpha 2\beta 1$/FAK/PI3K/AKT signaling pathway in vitro. Stem Cells Int 2023:2915826.
https://doi.org/10.1155/2023/2915826
20. Deng QQ, Lin P, Gu HL et al (2024) Silk protein-based nanoporous microsphere for controllable drug delivery through self-assembly in ionic liquid system. Biomacromolecules 25(3):1527–1540.
https://doi.org/10.1021/acs.biomac.3c01104
21. Taraballi F, Sushnitha M, Tsao C et al (2018) Biomimetic tissue engineering: tuning the immune and inflammatory response to implantable biomaterials. Adv Healthc Mater 7(17):1800490.
https://doi.org/10.1002/adhm.201800490
22. Chen HW, Lin MF (2020) Characterization, biocompatibility, and optimization of electrospun SF/PCL/CS composite nanofibers. Polymers 12(7):1439.
https://doi.org/10.3390/polym12071439
23. Ayaz F, Demir D, Bölgen N (2024) Electrospun nanofiber mats caged the mammalian macrophages on their surfaces and prevented their inflammatory responses independent of the fiber diameter. Sci Rep 14(1):12339.
https://doi.org/10.1038/s41598-024-61450-3
24. Singh AK, Pramanik K, Biswas A (2024) Constructing a biofunctionalized 3D-printed gelatin/sodium alginate/chitosan tripolymer complex scaffold with improvised biological and mechanical properties for bone-tissue engineering. Bio-Des Manuf 7(1):57–73.
https://doi.org/10.1007/s42242-023-00249-z
25. Ye YJ, Xu YF, Hou YB et al (2023) Regulation of tendon stem cell behavior by designed nanoporous topography of microfibers. Biomacromolecules 24(12):5859–5870.
https://doi.org/10.1021/acs.biomac.3c00896
26. Joukhdar H, Och Z, Tran H et al (2023) Imparting multi-scalar architectural control into silk materials using a simple multifunctional ice-templating fabrication platform. Adv Mater Technol 8(8):2201642.
https://doi.org/10.1002/admt.202201642
27. Wang LL, Lu GZ, Lu Q et al (2018) Controlling cell behavior on silk nanofiber hydrogels with tunable anisotropic structures. ACS Biomater Sci Eng 4(3):933–941.
https://doi.org/10.1021/acsbiomaterials.7b00969
28. Sensini A, Gualandi C, Focarete ML et al (2019) Multiscale hierarchical bioresorbable scaffolds for the regeneration of tendons and ligaments. Biofabrication 11(3):035026.
https://doi.org/10.1088/1758-5090/ab20ad
29. Cai JY, Liu J, Xu JJ et al (2023) Constructing high-strength nano-micro fibrous woven scaffolds with native-like anisotropic structure and immunoregulatory function for tendon repair and regeneration. Biofabrication 15(2):025002.
https://doi.org/10.1088/1758-5090/acb106
30. Calejo I, Costa-Almeida R, Reis RL et al (2019) A textile platform using continuous aligned and textured composite microfibers to engineer tendon-to-bone interface gradient scaffolds. Adv Healthc Mater 8(15):1900200.
https://doi.org/10.1002/adhm.201900200
31. Laranjeira M, Domingues RMA, Costa-Almeida R et al (2017) 3D mimicry of native-tissue-fiber architecture guides tendon-derived cells and adipose stem cells into artificial tendon constructs. Small 13(31):1700689.
https://doi.org/10.1002/smll.201700689
32. Russo V, El Khatib M, Prencipe G et al (2022) Tendon 3D scaffolds establish a tailored microenvironment instructing paracrine mediated regenerative amniotic epithelial stem cells potential. Biomedicines 10(10):2578.
https://doi.org/10.3390/biomedicines10102578
33. Ning C, Gao CJ, Li PX et al (2022) Dual-phase aligned composite scaffolds loaded with tendon-derived stem cells for Achilles tendon repair. Adv Ther 5(9):2200081.
https://doi.org/10.1002/adtp.202200081
34. Chen CH, Li DL, Chuang AD et al (2021) Tension stimulation of tenocytes in aligned hyaluronic acid/platelet-rich plasma-polycaprolactone core-sheath nanofiber membrane scaffold for tendon tissue engineering. Int J Mol Sci 22(20):11215.
https://doi.org/10.3390/ijms222011215
35. Wang Z, Lee WJ, Koh BH et al (2018) Functional regeneration of tendons using scaffolds with physical anisotropy engineered via microarchitectural manipulation. Sci Adv 4(10):eaat4537.
https://doi.org/10.1126/sciadv.aat4537
36. Teh TKH, Toh SL, Goh JCH (2013) Aligned fibrous scaffolds for enhanced mechanoresponse and tenogenesis of mesenchymal stem cells. Tissue Eng Part A 19(11–12):1360–1372.
https://doi.org/10.1089/ten.TEA.2012.0279
37. Giacomini F, Baião Barata D, Rho HS et al (2024) Microfluidically aligned collagen to maintain the phenotype of tenocytes in vitro. Adv Healthc Mater 13(6):2303672.
https://doi.org/10.1002/adhm.202303672

38. Calejo I, Labrador-Rached CJ, Gomez-Florit M et al (2022) Bioengineered 3D living fibers as in vitro human tissue models of tendon physiology and pathology. Adv Healthc Mater 11(15): 2102863. https://doi.org/10.1002/adhm.202102863
39. Maghdouri-White Y, Sori N, Petrova S et al (2021) Biomanufacturing organized collagen-based microfibers as a Tissue ENgineered Device (TEND) for tendon regeneration. Biomed Mater 16(2):025025. https://doi.org/10.1088/1748-605X/abb875
40. Chen CH, Chen SH, Kuo CY et al (2017) Response of dermal fibroblasts to biochemical and physical cues in aligned polycaprolactone/silk fibroin nanofiber scaffolds for application in tendon tissue engineering. Nanomaterials 7(8):219. https://doi.org/10.3390/nano7080219
41. Kent III RN, Jewett ME, Buck TP et al (2024) Engineered microenvironmental cues from fiber-reinforced hydrogel composites drive tenogenesis and aligned collagen deposition. Adv Healthc Mater 13(19):2400529. https://doi.org/10.1002/adhm.202400529
42. Xiao L, Sun YP, Liao L et al (2023) Response of mesenchymal stem cells to surface topography of scaffolds and the underlying mechanisms. J Mater Chem B 11(12):2550–2567. https://doi.org/10.1039/D2TB01875F
43. Chi JY, Wang MY, Chen JL et al (2022) Topographic orientation of scaffolds for tissue regeneration: recent advances in biomaterial design and applications. Biomimetics 7(3):131. https://doi.org/10.3390/biomimetics7030131
44. Adhikari J, Roy A, Chanda A et al (2023) Effects of surface patterning and topography on the cellular functions of tissue engineered scaffolds with special reference to 3D bioprinting. Biomater Sci 11(4):1236–1269. https://doi.org/10.1039/d2bm01499h
45. Donnaloja F, Raimondi MT, Messa L et al (2023) 3D photopolymerized microstructured scaffolds influence nuclear deformation, nucleo/cytoskeletal protein organization, and gene regulation in mesenchymal stem cells. APL Bioeng 7(3):036112. https://doi.org/10.1063/5.0153215
46. Tao SC, Huang JY, Li ZX et al (2021) Small extracellular vesicles with LncRNA H19 "overload": YAP regulation as a tendon repair therapeutic tactic. iScience 24(3):102200. https://doi.org/10.1016/j.isci.2021.102200
47. Lu JW, Yang XH, He CF et al (2023) Rejuvenation of tendon stem/progenitor cells for functional tendon regeneration through platelet-derived exosomes loaded with recombinant Yap1. Acta Biomater 161:80–99. https://doi.org/10.1016/j.actbio.2023.02.018